

Received January 30, 2018, accepted March 11, 2018, date of publication March 26, 2018, date of current version May 16, 2018.

Digital Object Identifier 10.1109/ACCESS.2018.2819600

A Comprehensive 3-Dimensional Random Mobility Modeling Framework for Airborne Networks

JUNFEI XIE¹, (Member, IEEE), YAN WAN², (Senior Member, IEEE), BAOQIAN WANG¹, SHENGLI FU³, (Senior Member, IEEE), KEJIE LU⁴, (Senior Member, IEEE), AND JAE H. KIM⁵, (Senior Member, IEEE)

¹Department of Computing Sciences, Texas A&M University-Corpus Christi, Corpus Christi, TX 78412, USA

²Department of Electrical Engineering, The University of Texas at Arlington, Arlington, TX 76019, USA

³Department of Electrical Engineering, University of North Texas, Denton, TX 76203, USA

⁴Department of Computer Science and Engineering, University of Puerto Rico at Mayagüez, Mayagüez 00681, Puerto Rico

⁵Boeing Research & Technology, Seattle, WA 98124-2207, USA

Corresponding author: Yan Wan (yan.wan@uta.edu)

This work was supported in part by the Texas Comprehensive Research Fund Program Grant and in part by the National Science Foundation under Grant CAREER-1714519, Grant CI-1730675 (CI-1730589, CI-1730570, and CI-1730325), and Grant CNS-1522458.

ABSTRACT To design and evaluate airborne networks (ANs), it is crucial to utilize random mobility models (RMMs) that capture the physical movement patterns of different aerial vehicles in real scenarios. Compared to expensive flight field tests, RMM-based modeling, simulation, and emulation is cost-effective with a large set of RMM-generated flight trajectories. Despite the importance of RMMs, we notice that most existing models focus on the 2-D movement, and do not consider the temporal and 3-D spatial correlation of aerial mobility patterns. In this paper, we propose a comprehensive 3-D smooth turn (ST) modeling framework for fixed-wing aircraft, which can serve as a design and evaluation foundation for future ANs. In the proposed framework, we develop two realistic 3-D ST RMMs that capture the diverse mobility patterns of fixed-wing aircraft, through coupling stochastic forcing with physical laws that govern the 3-D aerial maneuvers. We also develop two boundary models to determine the movement of aerial vehicles when they approach simulation boundaries. Moreover, we propose an approach to estimate the optimal 3-D ST RMMs, with which we can produce rich trajectory ensembles with statistical mobility patterns that match with the real trajectory data.

INDEX TERMS Modeling, parameter estimation, random mobility model, stochastic systems, unmanned aerial vehicles.

I. INTRODUCTION

Airborne networks (ANs) that use direct flight-to-flight communication are envisioned to be an important component of the next generation air transportation system, and are essential for applications that involve multiple cooperative unmanned aerial vehicles (UAV). With the proliferation of unmanned and manned aerial vehicles in the airspace, it is urgently needed to design an effective and robust AN to enable real-time information sharing required for safe maneuvering and effective coordination. Unlike ground vehicle/sensor networks with relatively low mobility and stable topology, aerial vehicles move fast in a 3-dimensional (3-D) airspace, change network topologies frequently, and are subject to stringent mechanical and aerodynamic constraints

to maintain safety. These unique properties lead to intricate difficulties for the design of ANs, and traditional networking protocols designed for ground vehicles/sensors cannot be directly used for these ANs.

Since flight field tests are usually cost-expensive, especially for large fixed-wing flights, random mobility models (RMMs) have been widely adopted to facilitate the design and evaluation of networking protocols. RMMs can produce a large number of flight trajectories as test cases for statistical performance evaluation. Existing simulation environments including EMANE/CORE, NS-3, and OPNET only support RMMs designed for ground vehicles/sensors-based Mobile Ad Hoc Networks (MANETs) [1]–[9]. Commonly used MANET RMMs include Random Walk [10], [11],

Random Waypoint [10], [12], and Random Direction [10], [13], [14]. In these models, the node trajectory does not reflect the real movement pattern as the nodes are assumed to be able to make sharp turns and directional changes abruptly. Therefore, these ground-based RMMs are not suitable for fixed-wing aircraft that demonstrate smooth turning behaviors. Considering the significant impact of RMMs on networking performance, it is important to develop a *realistic* RMM that captures the unique mobility attributes of aerial vehicles such as the temporal and 3-D spatial correlations that are subject to the safety requirement and mechanical and aerodynamic constraints.

In the literature, several AN-specific RMMs have recently been developed to capture the movement patterns of aerial vehicles in different scenarios. The Semi-Random Circular Movement (SRCM) model [15] abstracts the mobility of UAVs for the search and rescue mission, in which the potential location of the target is assumed to be known. In particular, the UAV is modeled to repeatedly circle around a fixed target location with different turn radii. The Three-Way Random and its extension, the Pheromone Repel model, have been developed for group reconnaissance missions [16]–[18]. They allow variable turn centers, and limit the possible values of the turn radius to $+r$, $-r$, and ∞ , where $r > 0$ is a constant. To realize that, they use a 3-state Markov chain to describe the motion of aircraft, and restrict the aircraft to take one of three states: go straight, turn left and turn right.

Although the aforementioned AN-specific RMMs can guarantee smooth turns, they place constraints on the turn center or turn radius, which are not typical in general aerial maneuvers. To achieve a flexible RMM for aerial vehicles, we developed a 2-D Smooth Turn (ST) RMM [19], [20], which allows aircraft to make smooth turns of varying turn centers and turn radii, and also captures the tendency of aircraft to go straight and make turns of large radii. Since its development, the 2-D ST RMM has been widely used for aerial networking studies (see e.g., [21]–[23]). Although this 2-D ST RMM captures smooth turns with flexible radii, it does not consider the aircraft dynamics along the vertical dimension and hence is insufficient to capture rich 3-D aerial maneuvers. A more comprehensive investigation of 3-D aerial movement patterns and the development of realistic 3-D AN-specific RMMs are needed to enable accurate evaluation and design of ANs in a 3-D airspace. Other AN-specific RMMs include the Flight-Plan based models [24] that record pre-defined trajectory plans and the Multi-Tier models [25] that incorporate multiple RMMs. Interested readers are recommended to read the survey paper [26] for a detailed discussion and comparison of these recently developed AN-specific RMMs.

Driven by the need of realistic 3-D AN-specific RMMs for aerial networking studies, we develop in this paper a comprehensive modeling framework with the following contributions:

- 1) *Realistic RMMs to capture smooth 3-D aerial mobility.*
We extend the basic 2-D ST RMM [19], [20] to the

3-D airspace. We develop two 3-D ST RMMs to capture different aerial mobilities along the vertical dimension. The first model assumes that the z -dimensional movement is independent from the movement on the horizontal plane. This model captures normal aerial maneuvers, mostly observed in civilian applications. The second model relaxes this assumption and captures the correlation of movement among all three dimensions. This model can thus describe military aircraft performing “high-g” turns. Furthermore, both models capture the correlation of accelerations across temporal and spatial directions during turns that comply with physical laws.

- 2) *A systematic procedure for parameter estimation.*
We develop a systematic procedure to estimate RMM parameters from real flight field test data. Statistical features of the resulting RMM match with those of flight field tests, and hence maximize the value of field tests. In particular, the resulting RMM can in turn produce a large number of trajectory ensembles to facilitate the evaluation and design of ANs. These ensembles follow the same statistics of the original flight field tests. The RMMs can also be used as uncertain mobility prediction models for the design of UAV mobility control strategies.
- 3) *Various model enhancements to support flexible and advanced user configuration.*
We also make several other generalizations to the 2-D ST mobility modeling framework. For instance, we allow the heading speed and turn radius in the 3-D ST RMMs to vary during each travel time interval, as compared to fixed constant values in the 2-D ST RMM. We also place mechanical and aerodynamic constraints and safety requirements for parameters in the model configuration. In addition, to capture realistic 3-D aerial mobility at simulation boundaries, we also develop new boundary models for the proposed 3-D ST RMMs.

In the rest of the paper, we first briefly review the 2-D ST RMM developed in our previous study in Section II. We then describe the two 3-D ST RMMs in Section III and elaborate on the realistic boundary models in Section IV. In Section V, we present the procedures to estimate model parameters from flight field test data and to configure random variables in the 3-D ST RMMs. Finally, we conclude the paper in Section VI.

II. REVIEW OF THE 2-D SMOOTH-TURN RANDOM MOBILITY MODEL

The 2-D ST RMM [19], [20] succinctly captures the mobility attributes of aerial vehicles moving in a 2-D airspace, through coupling stochastic forcing with physical dynamics. In this model, an aircraft randomly picks a turn center and circles around it with a constant heading speed for a randomly selected time period, τ_i , called travel time interval (see Figure 1 for an illustration). As the turn center is always on the line perpendicular to the heading direction, the generated flight trajectories are guaranteed to be smooth.

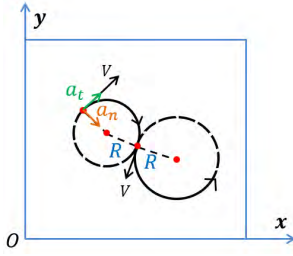


FIGURE 1. Illustration of the 2-D ST RMM and the directions of the tangential acceleration a_t and normal acceleration a_n .

The continuous-time dynamics of this model during the i -th travel time interval, τ_i , are described by the following equations:

$$\begin{aligned} a_t(t) &= 0 \\ a_n(t) &= \frac{V^2}{R(t)} \\ \dot{\phi}(t) &= -w(t) = -\frac{V}{R(t)} \\ \dot{p}_x(t) &= v_x(t) = V \cos(\phi(t)) \\ \dot{p}_y(t) &= v_y(t) = V \sin(\phi(t)) \end{aligned}$$

where $p_x(t)$, $p_y(t)$, $v_x(t)$ and $v_y(t)$ denote the x and y coordinates, and the velocities in x and y directions at time t , respectively. $w(t)$ is the angular velocity, and $\phi(t)$ represents the heading angle measured anti-clockwise. $a_t(t)$ and $a_n(t)$ are the tangential and normal accelerations, respectively. V is the heading speed, which is assumed to be a constant. $R(t) \in \mathcal{R}$ is the turn radius, with $R(t) > 0$ and $R(t) < 0$ representing right and left turns respectively. Both $w(t)$ and $R(t)$ are constants within the travel time interval τ_i . The inverse of $R(t)$ is assumed to follow a Gaussian distribution with a small variance σ^2 and zero mean. This distribution captures the tendency of aircraft to follow straight lines or make turns of large radii. The travel time interval τ_i is assumed to follow an exponential distribution with mean λ . This model can capture diverse moving patterns of fixed-wing aircraft, through configuring these three parameters V , λ , and σ^2 .

Other than accurately and succinctly capturing flexible random aircraft movement in a 2-D airspace, the 2-D ST RMM has many other appealing analytical properties. For instance, the *node distribution* is uniform, and hence leads to rich closed-form statistical results that are important for networking studies, such as the expected node degree and the probability for the network to be connected [19], [20].

Despite these advantages, the 2-D ST RMM cannot capture the mobility along the vertical dimension. In particular, the 2-D model is developed by analyzing two commonly observed aerial maneuvers: *cruise* [27] and *level coordinated turns* [28]. Cruise refers to the scenario when an aircraft moves along a straight line with a constant speed,¹ which

is achieved when balanced forces are applied onto the aircraft. The level coordinated turns describe an aircraft making steady and level turns with constant turn rate and heading speed, and are achieved when the aircraft has a non-zero constant bank angle [28] besides the balanced forces. Therefore, the 2-D ST RMM can not capture 3-D maneuvers such as climb, descend, steep turns, skidded turns, slipping turns, and spirals, etc [30], [31]. In addition, the 2-D ST RMM makes various assumptions to facilitate the closed-form analysis, such as the constant heading speed and simple boundary models. In this paper, we introduce two 3-D ST RMMs extended from this basic 2-D version to address the aforementioned limitations. The two 3-D models are more comprehensive and flexible for user configurations, and thus can be more convenient for the evaluation and design of ANs.

III. 3-D SMOOTH TURN RANDOM MOBILITY MODELS

In this section, we extend the basic 2-D ST RMM to 3-D by incorporating the features of 3-D aerial movement patterns. Two models are developed to capture different aerial maneuvers: 1) the *z-independent ST RMM* that captures nominal maneuvers in civilian applications, and 2) the *z-dependent ST RMM* that captures extreme maneuvers, such as those in air shows and military applications. Both models assume that an aircraft can be represented as a point mass, and all forces act on this point. Environmental effects such as wind and rain are not considered, as are commonly assumed in RMMs. The major difference between these two 3-D models lies in whether the aircraft mobility along the z direction is independent from that on the x - y plane.

A. z-INDEPENDENT ST RMM

The z -independent ST RMM assumes that the aircraft movement on the x - y plane is independent from that in the z direction. This assumption holds for aerial maneuvers that commonly appear in civilian applications, such as coordinated turns, cruise, climb, and descend [32]. Under this assumption, the aerial mobilities on the x - y plane and along the z direction can be analyzed separately, which significantly simplifies the analysis. In this model, the aircraft can vary its speed and altitude in the z direction. The dynamics on the x - y plane are similar to that in the basic 2-D ST RMM [19], [20]. The only difference is that the heading speed is allowed to vary in each travel time interval.

Let us analyze the underlying physical laws for aerial vehicles and succinctly capture those in the RMMs. In particular, the aircraft's tangential and normal accelerations on the x - y plane, denoted as $a_{xyt}(t)$ and $a_{xyn}(t)$ respectively, and its vertical acceleration, denoted as $a_z(t)$, can be described by the following equations [33]:

$$\begin{aligned} a_{xyt}(t) &= D(t) \cos(\alpha(t)) - L(t) \cos(\beta(t)) \sin(\alpha(t)) \\ a_{xyn}(t) &= L(t) \sin(\beta(t)) \\ a_z(t) &= L(t) \cos(\beta(t)) \cos(\alpha(t)) + D(t) \sin(\alpha(t)) - g \end{aligned}$$

¹The "speed" used in this paper refers to the airspeed, i.e., speed relative to the air [29].

where $D(t)$, $L(t)$, $\alpha(t)$, and $\beta(t)$ are the thrust-drag acceleration, lift acceleration, pitch angle, and roll angle at time t . g is the gravity acceleration and is assumed to be a constant. $D(t)$, $L(t)$, $\beta(t)$ and $\alpha(t)$ are constants for each maneuver within each travel time interval τ_i . Therefore, $a_{xyn}(t)$, $a_{xyt}(t)$ and $a_z(t)$ are also constants within each travel time interval. Note that when $a_{xyt}(t) = 0$, the aircraft turns with a constant heading speed. When $a_{xyt}(t) \neq 0$, the vehicle's heading speed is allowed to vary. Based on whether $a_{xyt}(t) = 0$ or not within each τ_i , we develop two z -independent ST RMMs with either a constant or variable horizontal heading speed.

1) CONSTANT HORIZONTAL HEADING SPEED

In this case, $a_{xyt}(t) = 0$, and both $a_{xyn}(t)$ and $a_z(t)$ are constants within each travel time interval τ_i . This leads to the heading speed $V_{xy}(t)$, turn radius $R_{xy}(t)$, and angular velocity $w_{xy}(t)$, all being constants within each travel time interval τ_i . The continuous-time dynamics of this 3-D ST RMM model within each τ_i are then captured by the following equations:

$$\begin{aligned} a_{xyt}(t) &= 0 \\ a_{xyn}(t) &= \frac{V_{xy}^2(t)}{R_{xy}(t)} \\ \dot{\phi}_{xy}(t) &= -w_{xy}(t) = -\frac{V_{xy}(t)}{R_{xy}(t)} \\ \dot{p}_x(t) &= v_x(t) = V_{xy}(t) \cos(\phi_{xy}(t)) \\ \dot{p}_y(t) &= v_y(t) = V_{xy}(t) \sin(\phi_{xy}(t)) \end{aligned} \quad (1)$$

The aerial motion along the z -direction can be described by

$$\ddot{p}_z(t) = \dot{v}_z(t) = a_z(t),$$

where $p_z(t)$ and $v_z(t)$ represent the z coordinate and vertical speed of the aircraft at time t , respectively. The turn radius can be negative values to represent left turns. Similar to the 2-D ST model, at the end of the $(i-1)$ -th travel time interval, we randomly select a new set of values for the following random variables: travel time interval τ_i , heading speed V_{xy} , turn radius R_{xy} , and vertical acceleration a_z . The modeling of the switching of heading speeds $V_{xy}(t)$ using the thrust-drag force is neglected at the end of a travel time interval, to be consistent with the practice in the RMM literature.

The discrete-time model obtained through sampling (1) at every small sampling time Δt is as follows:

$$\begin{aligned} c_x[T_i] &= p_x[T_i] + R_{xy}[T_i] \sin(\phi_{xy}[T_i]) \\ c_y[T_i] &= p_y[T_i] - R_{xy}[T_i] \cos(\phi_{xy}[T_i]) \\ \phi_{xy}[k+1] &= \phi_{xy}[k] - \theta - 2\pi \left\lfloor \frac{\phi_{xy}[k] - \theta}{2\pi} \right\rfloor \\ p_x[k+1] &= c_x[T_i] - R_{xy}[T_i] \sin(\phi_{xy}[k+1]) \\ p_y[k+1] &= c_y[T_i] + R_{xy}[T_i] \cos(\phi_{xy}[k+1]) \end{aligned} \quad (2)$$

and

$$p_z[k+1] = p_z[k] + a_z[T_i] \Delta t.$$

where T_i and T_{i+1} define the start and end times of the i -th travel time interval, i.e., $T_{i+1} - T_i = \tau_i$. $\theta = w_{xy}[T_i] \Delta t = \frac{V_{xy}[T_i]}{R_{xy}[T_i]} \Delta t$ is the turn angle at each time instance $k \Delta t$, and

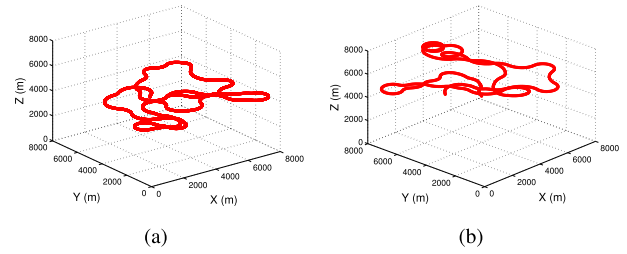


FIGURE 2. Example trajectories generated by the z -independent ST RMM with a) constant horizontal heading speed within each travel time interval τ_i , and b) variable horizontal heading speed within each travel time interval τ_i .

$T_i \leq k \Delta t \leq T_{i+1}$, $k \in \mathbb{Z}^+$. $c_x[T_i]$ and $c_y[T_i]$ represent the x and y coordinates of the turn center, denoted as $\mathbf{p}_{cxy}[T_i]$, at time instance T_i respectively. An example trajectory generated by this model is shown in Figure 2(a).

2) VARIABLE HORIZONTAL HEADING SPEED

When $a_{xyt}(t) \neq 0$, the horizontal heading speed $V_{xy}(t)$ varies over time. $a_{xyn}(t)$, $a_{xyt}(t)$ and $a_z(t)$ remain to be constants within each travel time interval. Then the continuous-time dynamics of this model can be described using Equation (1), with $a_{xyt}(t)$ changed to $\dot{V}_{xy}(t)$. At the end of the $(i-1)$ -th travel time interval, T_i , the set of random variables to be updated include the travel time interval τ_i , heading speed V_{xy} , turn radius R_{xy} , vertical acceleration a_z and horizontal tangential acceleration a_{xyt} .

The discrete-time dynamics are described by the following equations, assuming that Δt is small enough:

$$\begin{aligned} a_{xyn}[T_i] &= \frac{V_{xy}^2[T_i]}{R_{xy}[T_i]} \\ V_{xy}[k+1] &= a_{xyt}[T_i] \Delta t + V_{xy}[k] \\ R_{xy}[k] &= \frac{V_{xy}^2[k]}{a_{xyn}[T_i]} \\ \theta[k] &= \frac{V_{xy}[k]}{R_{xy}[k]} \Delta t \\ c_x[k] &= p_x[k] + R_{xy}[k] \cos(\phi_{xy}[k]) \\ c_y[k] &= p_y[k] - R_{xy}[k] \sin(\phi_{xy}[k]) \\ \phi_{xy}[k+1] &= \phi_{xy}[k] - \theta[k] - 2\pi \left\lfloor \frac{\phi_{xy}[k] - \theta[k]}{2\pi} \right\rfloor \\ p_x[k+1] &= c_x[k] - R_{xy}[k] \cos(\phi_{xy}[k+1]) \\ p_y[k+1] &= c_y[k] + R_{xy}[k] \sin(\phi_{xy}[k+1]) \end{aligned} \quad (3)$$

and

$$p_z[k+1] = p_z[k] + a_z[T_i] \Delta t.$$

An example trajectory generated by this model is shown in Figure 2(b).

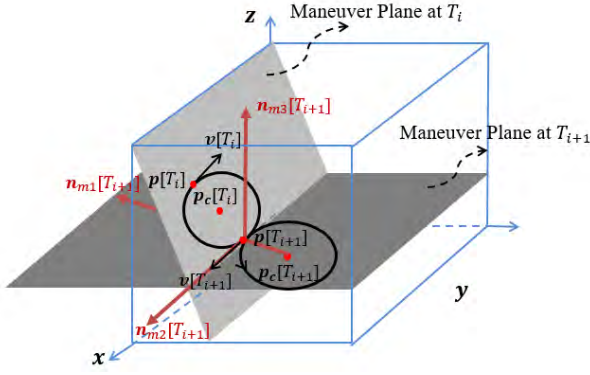


FIGURE 3. Illustration of the z -dependent ST RMM and the maneuver planes. $\mathbf{n}_{m1}[T_{i+1}]$, $\mathbf{n}_{m2}[T_{i+1}]$, $\mathbf{n}_{m3}[T_{i+1}]$ are unit vectors that define the maneuver plane at T_{i+1} .

B. z -DEPENDENT ST RMM

The z -dependent ST RMM captures the correlation of an aircraft's motion across the x , y and z directions, and hence is useful for aerial maneuvers such as climbing and descending turns. This correlation is captured through the introduction of a *maneuver plane* uniquely determined by the aircraft's tangential and normal acceleration vectors [34]. The key idea is that an aircraft circles around a randomly selected turn center on the maneuver plane for a randomly selected duration before it chooses a new maneuver plane and a new turn center (see Figure 3 for an illustration). The new turn center is on the plane perpendicular to the current heading direction. This perpendicularity guarantees the smoothness of turns.

The tangential and normal accelerations on the maneuver plane can be described by the following equations:

$$a_t(t) = D(t) - g \sin(\alpha(t))$$

$$a_n(t) = L(t) \sin(\beta(t))$$

Within each travel time interval, the forces perpendicular to the maneuver plane add up to zero, i.e., $L(t) \cos(\beta(t)) - g \cos(\alpha(t)) = 0$, and hence the aircraft remains on this maneuver plane during this entire interval. $a_t(t)$ and $a_n(t)$ are also constants within each travel time interval. At the end of each travel time interval, the maneuver plane changes and the velocity vector is on the line intersecting the old and new maneuver planes. The modeling of the switching of maneuver planes using the bank angle and lift force is neglected, to be consistent with the practice in the RMM literature.

The dynamics of this model can be captured by similar equations as shown in the z -independent ST RMMs. The difference is that the maneuver on the x - y plane is moved to the maneuver plane. In particular, within each travel time interval, the aerial mobility in the maneuver coordinate frame (determined by the maneuver plane and its normal vector) can be described by Equation (2) when $a_t(t) = 0$, and Equation (3), otherwise. Then the dynamics in the inertial coordinate frame can be obtained through coordinate transformation.

Now we describe the key steps to determine the velocity vector and turn center, and hence the maneuver plane and the maneuver coordinate frame. Specifically, at the end of the $(i-1)$ -th travel time interval T_i , the aircraft randomly selects a new heading speed $V[T_i]$ (without changing the direction), and a new turn center $\mathbf{p}_c[T_i] = [c_x[T_i], c_y[T_i], c_z[T_i]]'$ on the plane perpendicular to its velocity direction, where superscript $'$ denotes the transposition operator. This new turn center is uniquely determined by a randomly selected new turn radius $R[T_i]$ and altitude of the new turn center $c_z[T_i]$. Mathematically, the position of the new turn center $\mathbf{p}_c[T_i]$ can be determined by solving the following equations:

$$\begin{aligned} \mathbf{v}[T_i] \cdot (\mathbf{p}_c[T_i] - \mathbf{p}[T_i]) &= 0 \\ \|\mathbf{p}_c[T_i] - \mathbf{p}[T_i]\| &= R[T_i] \end{aligned} \quad (4)$$

where $\|\mathbf{x}\|$ represents the euclidean norm of vector \mathbf{x} . Solutions exist when

$$p_z[T_i] - K \leq c_z[T_i] \leq p_z[T_i] + K \quad (5)$$

where $K = \frac{R[T_i] \sqrt{V^2[T_i] - v_z^2[T_i]}}{V[T_i]}$. $\mathbf{p}[T_i] = [p_x[T_i], p_y[T_i], p_z[T_i]]'$, $\mathbf{v}[T_i] = [v_x[T_i], v_y[T_i], v_z[T_i]]'$ denote the aircraft's position and velocity vectors in the inertial coordinate frame, respectively. Note that Equation (4) has two solutions. We here randomly select one as the new turn center. Then the new maneuver plane can be uniquely determined by $\mathbf{p}_c[T_i]$ and $\mathbf{v}[T_i]$. We define the maneuver coordinate frame using the following unit vectors (see Figure 3 for an illustration) measured in the inertial coordinate frame:

$$\begin{aligned} \mathbf{n}_{m1}[T_i] &= \begin{cases} \frac{\mathbf{p}_c[T_i] - \mathbf{p}[T_i]}{\|\mathbf{p}_c[T_i] - \mathbf{p}[T_i]\|}, & \text{for right turns} \\ -\frac{\mathbf{p}_c[T_i] - \mathbf{p}[T_i]}{\|\mathbf{p}_c[T_i] - \mathbf{p}[T_i]\|}, & \text{for left turns} \end{cases} \\ \mathbf{n}_{m2}[T_i] &= \frac{\mathbf{v}[T_i]}{\|\mathbf{v}[T_i]\|}, \\ \mathbf{n}_{m3}[T_i] &= \mathbf{n}_{m1}[T_i] \times \mathbf{n}_{m2}[T_i], \end{aligned}$$

where $\mathbf{p}[T_i]$ is the original point. Denote $\mathbf{n}_1 = [1, 0, 0]'$, $\mathbf{n}_2 = [0, 1, 0]'$, and $\mathbf{n}_3 = [0, 0, 1]'$ as the unit vectors in the x , y and z directions of the inertial coordinate frame. The aircraft's location $\mathbf{p}_m[T_i]$ and velocity $\mathbf{v}_m[T_i] = [v_{m1}[T_i], v_{m2}[T_i], v_{m3}[T_i]]'$ represented in the maneuver coordinate frame can be projected onto the inertial coordinate frame by using the following equations

$$\begin{aligned} \mathbf{p}[T_i] &= \begin{bmatrix} \mathbf{n}_1 \cdot \mathbf{n}_{m1}[T_i] & \mathbf{n}_1 \cdot \mathbf{n}_{m2}[T_i] & \mathbf{n}_1 \cdot \mathbf{n}_{m3}[T_i] \\ \mathbf{n}_2 \cdot \mathbf{n}_{m1}[T_i] & \mathbf{n}_2 \cdot \mathbf{n}_{m2}[T_i] & \mathbf{n}_2 \cdot \mathbf{n}_{m3}[T_i] \\ \mathbf{n}_3 \cdot \mathbf{n}_{m1}[T_i] & \mathbf{n}_3 \cdot \mathbf{n}_{m2}[T_i] & \mathbf{n}_3 \cdot \mathbf{n}_{m3}[T_i] \end{bmatrix} \\ &\quad \times (\mathbf{p}_m[T_i] - \mathbf{o}_m[T_i]) \\ \mathbf{v}[T_i] &= v_{m1}[T_i] \mathbf{n}_{m1}[T_i] + v_{m2}[T_i] \mathbf{n}_{m2}[T_i] \\ &\quad + v_{m3}[T_i] \mathbf{n}_{m3}[T_i] \end{aligned}$$

where \cdot represents the dot product operator. $\mathbf{o}_m[T_i]$ is the coordinate of $\mathbf{p}[T_i]$ projected onto the maneuver coordinate

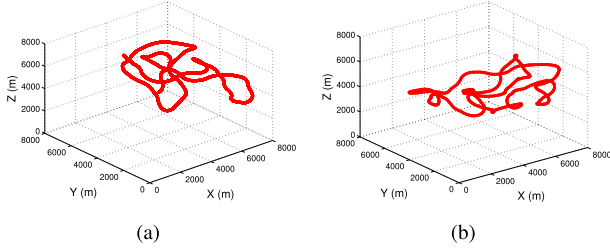


FIGURE 4. Example trajectories generated by the z -dependent ST RMM with a) constant and b) variable heading speed.

frame and

$$\mathbf{o}_m[T_i] = - \begin{bmatrix} \mathbf{p}[T_i] \cdot \mathbf{n}_{m1}[T_i] \\ \mathbf{p}[T_i] \cdot \mathbf{n}_{m2}[T_i] \\ \mathbf{p}[T_i] \cdot \mathbf{n}_{m3}[T_i] \end{bmatrix}$$

Figure 4 shows example trajectories generated by this model.

In the case when $a_t(t) = 0$, instead of frequently switching between the maneuver and inertial coordinate frames, we can also directly calculate the aircraft's motion in the inertial coordinate frame. In particular, the continuous-time dynamics of this model within each τ_i with $a_t(t) = 0$ can be described by the following equations,

$$\begin{aligned} \dot{\mathbf{p}}(t) &= \mathbf{v}(t) \\ \dot{\mathbf{v}}(t) &= \mathbf{a}(t) \\ \mathbf{v}(t) &= \mathbf{\Omega}(t) \times (\mathbf{p}(t) - \mathbf{p}_c(t)) \\ \mathbf{a}(t) &= \dot{\mathbf{\Omega}}(t) \times (\mathbf{p}(t) - \mathbf{p}_c(t)) + \dot{\mathbf{\Omega}}(t) \times (\dot{\mathbf{p}}(t) - \dot{\mathbf{p}}_c(t)) \end{aligned}$$

where $\mathbf{a}(t) = [a_x(t), a_y(t), a_z(t)]'$ is the acceleration vector, $\mathbf{\Omega}(t)$ is the turn rate vector with magnitude $w(t) = \|\mathbf{\Omega}(t)\| = \frac{a_m(t)}{V(t)} = \frac{V(t)}{R(t)}$, $V(t) = \|\mathbf{v}(t)\|$, and $R(t)$ is the turn radius. The symbol \times denotes the vector cross product operator. As $a_t(t) = 0$ and $a_m(t)$ is a constant within each travel time interval τ_i , we have $\dot{\mathbf{\Omega}}(t) = 0$. Furthermore, as $\mathbf{p}_c(t)$ is fixed, we have $\dot{\mathbf{p}}_c(t) = 0$ and hence $\mathbf{a}(t) = \mathbf{\Omega}(t) \times \mathbf{v}(t)$. Then the derivative of $\mathbf{a}(t)$ can be calculated as

$$\dot{\mathbf{a}}(t) = \dot{\mathbf{\Omega}}(t) \times \mathbf{v}(t) + \mathbf{\Omega}(t) \times \dot{\mathbf{v}}(t) = -w^2(t)\mathbf{v}(t)$$

We can now obtain the state-space dynamics of aircraft within each travel time interval as follows

$$\dot{\mathbf{x}}(t) = \begin{bmatrix} \mathbf{0}_{3 \times 3} & I & \mathbf{0}_{3 \times 3} \\ \mathbf{0}_{3 \times 3} & \mathbf{0}_{3 \times 3} & I \\ \mathbf{0}_{3 \times 3} & -w^2(t)I & \mathbf{0}_{3 \times 3} \end{bmatrix} \mathbf{x}(t)$$

where the state $\mathbf{x}(t) = [\mathbf{p}'(t), \mathbf{v}'(t), \mathbf{a}'(t)]'$, and $I \in \mathbb{R}^{3 \times 3}$ is an identity matrix. The discrete-time model is given by

$$\begin{aligned} w[T_i] &= \frac{V[T_i]}{R[T_i]} \\ \mathbf{x}[k+1] &= \begin{bmatrix} 1 & \frac{\sin(\theta)}{w[T_i]} & \frac{1 - \cos(\theta)}{w^2[T_i]} \\ 0 & \cos(\theta) & \frac{\sin(\theta)}{w[T_i]} \\ 0 & -w[T_i] \sin(\theta) & \cos(\theta) \end{bmatrix} \otimes I \mathbf{x}[k] \end{aligned}$$

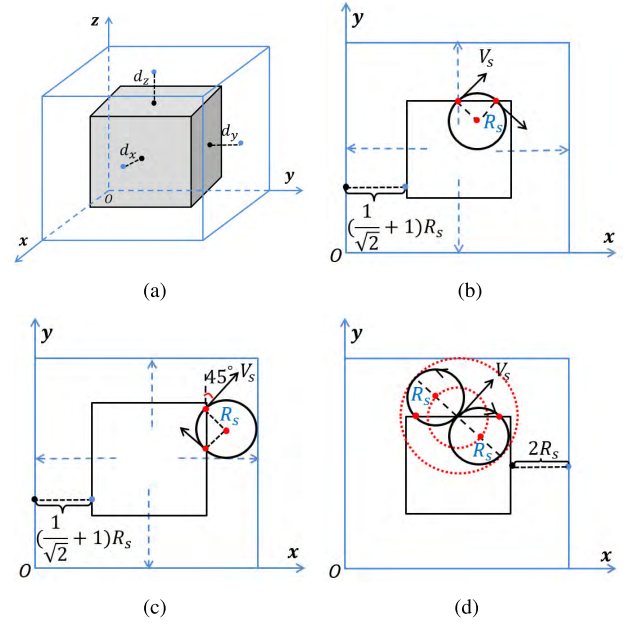


FIGURE 5. Illustration of the a) buffer zone, which is the area between the blue and the grey cubes, b)-c) boundary model for the z -independent mobility model, which requires $d_x = d_y = (1 + \frac{1}{\sqrt{2}})R_s$, $d_z = \frac{v_{zmax}^2}{2a_{zmax}}$ to ensure that the aircraft stays within the simulation area, and d) boundary model for the z -dependent ST RMM, which requires $d_x = d_y = d_z = 2R_s$ to ensure that the aircraft stays within the simulation area.

where $\theta = w[T_i]\Delta t$ is the turn angle within each time instance. \otimes is the kronecker product.

IV. REALISTIC BOUNDARY MODELS

In the basic 2-D ST RMM, we applied the canonical “wrap-around” model [14] and the “reflection” model [35] to describe aerial mobilities close to boundaries. Both boundary models demonstrate sharp directional changes that are not observed in realistic fixed-wing aerial trajectories. In this section, we design boundary models for the 3-D ST RMMs, by adopting the “buffer zone” idea used in the Gauss-Markov [10], [35] and Reconnaissance RMMs [16]–[18].

The buffer zone is defined as the area between the simulation boundary (blue cube) and the inner zone (grey cube) shown in Figure 5(a), where d_x, d_y, d_z determine the depth of the buffer zone. The key idea of this boundary model is that once an aircraft reaches the buffer zone, it switches immediately to a new motion pattern until it moves out of the buffer zone. The boundary models for the z -independent and z -dependent ST RMMs differ slightly due to the aerial motion along the vertical direction as discussed below.

A. BOUNDARY MODEL FOR THE z -INDEPENDENT ST RMM

In the boundary model for the z -independent ST RMM, the motion pattern on the x - y plane when an aircraft approaches the boundary can be described by Figure 5(b). In particular, once an aircraft reaches the buffer zone, assuming at time k_b , it checks its heading direction with respect to

the boundary, reselects a new turn radius R_s and speed V_s (without changing the direction), and sets $a_{xyt}[k_b]$ to zero, if $a_{xyt}[k_b] \neq 0$. If its heading is to the right of the vector normal to the boundary, the aircraft turns clockwise until it moves out of the buffer zone, otherwise it turns anticlockwise. R_s is selected as the minimum safe turn radius of this aircraft type (see configuration of R_s in Section V for reference). Alternatively, we can also set R_s as the minimum safe turn radius associated with the particular speed when the aircraft reaches the buffer zone, i.e., $V_{xy}[k_b]$. In this case, the aircraft does not reselect the speed, i.e., $V_s = V_{xy}[k_b]$. To ensure that the aircraft does not cross the boundary, the minimum depths of the buffer along the x and y directions are $d_x = d_y = (1 + \frac{1}{\sqrt{2}})R_s$ (see Figure 5(c) for the illustration).

To analyze the motion pattern along the z -direction, we first introduce some notations. Define $a_{zmax} = \max\{|a_z[k]|\}$ and $v_{zmax} = \max\{|v_z[k]|\}$. When the aircraft reaches the buffer zone near the ceiling, it chooses $a_z[k_b]$ from the range of $(-a_{zmax}, -\frac{2d_z}{v_z[k_b]})$, where $v_z[k_b]$ is the vertical speed when the aircraft enters the buffer zone at time k_b . Similarly, when the aircraft reaches the buffer zone near the bottom, it chooses a_z from the range of $(\frac{2d_z}{v_z[k_b]}, a_{zmax})$. It's easy to prove that the minimum buffer depth d_z required to keep the aircraft within the simulation area is $\frac{v_{zmax}^2}{2a_{zmax}}$.

B. BOUNDARY MODEL FOR THE z -DEPENDENT ST MOBILITY MODEL

For the z -dependent ST RMM, the aircraft can follow similar motion patterns adopted in the z -independent ST RMM on the x - y plane when it reaches the buffer zone. To determine whether the aircraft should turn clockwise or anticlockwise, we need to find the intersection of the maneuver plane and the buffer zone, which can be complex. For simplicity, we increase the depths of the buffer zone to $d_x = d_y = d_z = 2R_s$. It can be proved that this depth allows the aircraft to turn in either directions without leaving the simulation area (see Figure 5(d) for an illustration).

V. ESTIMATION USING REAL FLIGHT FIELD TEST DATA

In this section, we provide a procedure to estimate random variables in the 3-D ST RMMs from real flight field test data. This procedure produces a realistic RMM with the same statistics as those of the real flight trajectories. The field test data we use in this study include two trajectories of the Tempest fixed-wing UAV (see Figure 6). These two trajectories, denoted as A and B last for about 3 and 5 minutes respectively. Each trajectory dataset consists of 3-D global GPS positions of the UAV (measured by latitude ϕ , longitude λ , and altitude h) tagged with their measurement time points. The estimation procedure includes four major steps: 1) data preparation, 2) estimation of trajectory-specific random variable values, 3) estimation of a key threshold, and 4) estimation of parameters in model random variables. Next we illustrate the steps for estimating both the z -independent (with $a_{txy}(t) = 0$) and the z -dependent (with $a_t(t) = 0$) ST RMMs. Similar

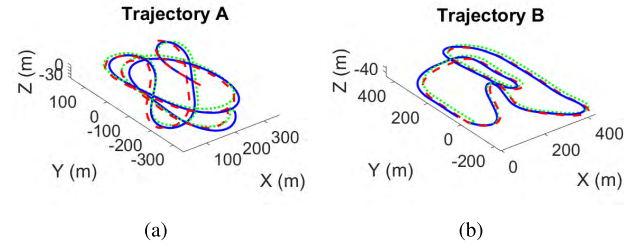


FIGURE 6. Real flight trajectories: a) A and b) B. The blue solid curves represent the flight field test data after conversion, resampling and smoothing. The green dotted and red dashed curves are estimated trajectories using the z -independent and z -dependent ST RMMs, respectively.

procedures apply for the cases when the tangential acceleration is not zero.

A. DATA PREPARATION

The data preparation step consists of two steps: 1) *coordinate transformation* to convert data into the navigation coordinates; and 2) *data preprocessing* to clean the data and remove noises.

1) COORDINATE TRANSFORMATION

The conversion from the GPS locations (ϕ, λ, h) to the navigation (east-north-up, ENU) coordinates (p_e, p_n, p_u), is achieved through two steps. The first step is to convert the GPS locations to the earth-centered earth-fixed (ECEF) coordinates (X, Y, Z) using the following equations [36]–[38]:

$$\begin{aligned} X &= (N(\phi) + h) \cos(\phi) \cos(\lambda) \\ Y &= (N(\phi) + h) \cos(\phi) \sin(\lambda) \\ Z &= (N(\phi)(1 - e^2) + h) \sin(\phi) \end{aligned}$$

where $a = 6378137$ and $e^2 = 0.0067$ are the semi-major axis and the first numerical eccentricity of the ellipsoid, respectively. $N(\phi) = \frac{a}{\sqrt{1 - e^2 \sin^2(\phi)}}$ is the distance from the surface to the z -axis along the ellipsoid normal.

The second step is to convert the ECEF coordinates to the ENU coordinates:

$$\begin{bmatrix} p_e \\ p_n \\ p_u \end{bmatrix} = \begin{bmatrix} -\sin(\lambda) & \cos(\lambda) & 0 \\ -\sin(\phi) \cos(\lambda) & -\sin(\phi) \sin(\lambda) & \cos(\phi) \\ \cos(\phi) \cos(\lambda) & \cos(\phi) \sin(\lambda) & \sin(\phi) \end{bmatrix} \begin{bmatrix} X - X_r \\ Y - Y_r \\ Z - Z_r \end{bmatrix}$$

where (X_r, Y_r, Z_r) represents the reference point, which is the starting location in each dataset.

2) DATA PREPROCESSING

As the sampling rate of the flight field test data is not consistent over time, we resample the data every $\Delta t = 0.1$ s. We then filter the data using the “moving average” algorithm [39] with 100 points used in the average operation to remove noises. The resulting flight location data are then denoted as $\mathbf{p}[k] = [p_x[k], p_y[k], p_z[k]]'$, shown in the blue solid curves in Figure 6.

TABLE 1. Random variables to be estimated.

Model	Random Variables
z -independent ($a_{txy}(t) = 0$)	$R_{xy}, V_{xy}, a_z, \tau$
z -dependent ($a_t(t) = 0$)	R, V, c_z, τ

B. ESTIMATION OF TRAJECTORY-SPECIFIC RANDOM VARIABLE VALUES

This step aims to estimate values of the random variables in the 3-D ST RMMs (see the list of random variables involved in each model in Table 1). Two substeps are involved. The first substep is to extract values of random variables at each time instance. The second substep is to estimate values of random variables during each travel time interval.

1) EXTRACTION OF RANDOM VARIABLE VALUES AT EACH TIME INSTANCE

We extract values of velocity $\mathbf{v}[k] = [v_x[k], v_y[k], v_z[k]]'$, turn radius $R[k]$ (or $R_{xy}[k]$), turn rate $w[k]$ (or $w_{xy}[k]$), turn center $\mathbf{p}_c = [c_x[k], c_y[k], c_z[k]]'$ (or $\mathbf{p}_{cxy} = [c_x[k], c_y[k]]'$) and vertical acceleration $a_z[k]$ at each time instance. In particular,

$$\begin{aligned}\mathbf{v}[k] &= (\mathbf{p}[k+1] - \mathbf{p}[k])/\Delta t \\ a_z[k] &= (v_z[k+1] - v_z[k])/\Delta t\end{aligned}$$

The values for the other random variables are extracted differently for the z -independent and z -dependent ST RMMs.

For the z -independent ST RMM, the position and velocity data along the x and y directions are used to calculate $R_{xy}[k]$ and $w_{xy}[k]$. Specifically, we first derive the turn center $\mathbf{p}_{cxy}[k]$ by fitting the trajectory with 2-D circles, using two adjacent locations and velocity vectors on the x - y plane, i.e., $(p_x[k], p_y[k])$, $(p_x[k+1], p_y[k+1])$, $(v_x[k], v_y[k])$, and $(v_x[k+1], v_y[k+1])$. The turn radius $R_{xy}[k]$ and turn rate $w_{xy}[k]$ are then calculated as

$$\begin{aligned}R_{xy}[k] &= \sqrt{(p_x[k] - c_x[k])^2 + (p_y[k] - c_y[k])^2} \\ w_{xy}[k] &= V_{xy}[k]/R_{xy}[k] \\ V_{xy}[k] &= \sqrt{v_x^2[k] + v_y^2[k]}\end{aligned}$$

For the z -dependent ST RMM, the turn center is found in a similar way, i.e., by fitting the trajectory with 3-D circles using 3-D location and velocity vectors at two adjacent time instances. The turn radius $R[k]$ and turn rate $w[k]$ are then calculated as

$$\begin{aligned}R[k] &= \|\mathbf{p}[k] - \mathbf{p}_c[k]\| \\ w[k] &= V[k]/R[k] \\ V[k] &= \sqrt{v_x^2[k] + v_y^2[k] + v_z^2[k]}\end{aligned}$$

2) ESTIMATION OF RANDOM VARIABLE VALUES DURING EACH TRAVEL TIME INTERVAL

As the speed and turn radius are constants during each travel time interval for both the z -independent (with $a_{txy}(t) = 0$)

and z -dependent (with $a_t(t) = 0$) ST RMMs, we can determine the length of each travel time interval based on either speed or turn radius. We here choose the turn radius, which is assumed to be independent over different travel time intervals. In particular, starting from the initial time $k = 0$, we scan the turn radius $R[k]$ (or $R_{xy}[k]$) at each time instance until the change of $R[k]$ (or $R_{xy}[k]$) exceeds a threshold R^{thrd} (or R_{xy}^{thrd}) or its sign switches at time k . Note that positive (or negative) turn radius represents right (or left) turns. Then the first travel time interval $\hat{\tau}_1 = k$. This process repeats till the last time instance. We here use \hat{T}_i and \hat{T}_{i+1} to represent the starting and end time of the estimated i -th travel time interval. The values of the random variables during each travel time interval in the z -independent ST RMM can be estimated as

$$\begin{aligned}\hat{\tau}_i &= \hat{T}_{i+1} - \hat{T}_i \\ \hat{V}_{xy}[\hat{T}_i] &= \frac{1}{\hat{\tau}_i} \sum_{k=\hat{T}_i}^{\hat{T}_{i+1}} V_{xy}[k] \\ \hat{R}_{xy}[\hat{T}_i] &= \frac{1}{\hat{\tau}_i} \sum_{k=\hat{T}_i}^{\hat{T}_{i+1}} \hat{R}_{xy}[k] \\ \hat{a}_z[\hat{T}_i] &= (v_z[\hat{T}_{i+1}] - v_z[\hat{T}_i])/\hat{\tau}_i\end{aligned}$$

The turn rate during $\hat{\tau}_i$ can be computed by $\hat{w}_{xy}[\hat{T}_i] = \frac{\hat{V}_{xy}[\hat{T}_i]}{\hat{R}_{xy}[\hat{T}_i]}$.

For the z -dependent ST RMM, the values of the random variables can be estimated similarly,

$$\begin{aligned}\hat{V}[\hat{T}_i] &= \frac{1}{\hat{\tau}_i} \sum_{k=\hat{T}_i}^{\hat{T}_{i+1}} V[k] \\ \hat{R}[\hat{T}_i] &= \frac{1}{\hat{\tau}_i} \sum_{k=\hat{T}_i}^{\hat{T}_{i+1}} \hat{R}[k] \\ \hat{c}_z[\hat{T}_i] &= c_z[\hat{T}_i]\end{aligned}$$

and $\hat{w}[\hat{T}_i] = \frac{\hat{V}[\hat{T}_i]}{\hat{R}[\hat{T}_i]}$.

We note that the estimated values of these random variables can be further used to estimate the location and velocity of the aircraft at each time instance $k \in [\hat{T}_i, \hat{T}_{i+1}]$, denoted as $\hat{\mathbf{p}}[k] = [\hat{p}_x[k], \hat{p}_y[k], \hat{p}_z[k]]'$ and $\hat{\mathbf{v}}[k] = [\hat{v}_x[k], \hat{v}_y[k], \hat{v}_z[k]]'$. Figure 6 shows the estimated trajectories using the z -independent (red dashed curves) and z -dependent (green dotted curves) ST RMMs. Figure 7 shows the estimated turn rate $\hat{w}_{xy}[\hat{T}_i]$, horizontal speed $\hat{V}_{xy}[\hat{T}_i]$ and vertical acceleration $\hat{a}_z[\hat{T}_i]$ for the dataset A using z -independent ST RMM. Figure 8 shows the estimated turn rate $\hat{w}[\hat{T}_i]$ and speed $\hat{V}[\hat{T}_i]$ for the same dataset using the z -dependent ST RMM. The threshold R^{thrd} (or R_{xy}^{thrd}) used to generate these figures adopts the values listed in Table 2. Of note, the speed trajectory shown in Figure 7(b) is very close to the one shown in Figure 8(b), as the vertical speed $v_z[k]$ in dataset A is small.

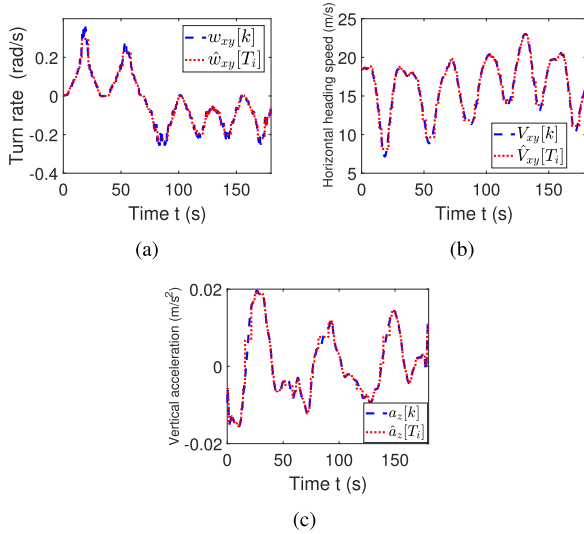


FIGURE 7. Comparison of the estimated a) turn rate $\hat{w}_{xy}[\hat{T}_i]$, b) horizontal heading speed $\hat{V}_{xy}[\hat{T}_i]$, and c) vertical acceleration $\hat{a}_z[\hat{T}_i]$ during each travel time interval with the associated values extracted at each time instance from the field test dataset A using the z-independent ST RMM.

TABLE 2. Values of thresholds selected for each trajectory.

Trajectories	R_{xy}^{thrd} (z-independent)	R^{thrd} (z-dependent)
A	34m	800m
B	10m	550m

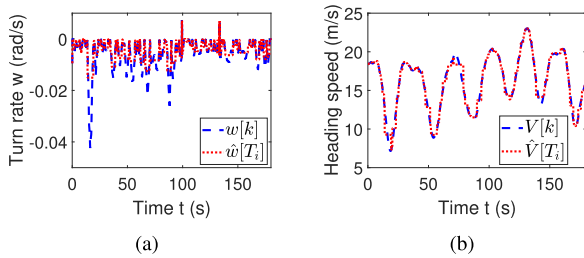


FIGURE 8. Comparison of the estimated a) turn rate $\hat{w}[\hat{T}_i]$ and b) heading speed $\hat{V}[\hat{T}_i]$ during each travel time interval with the associated values extracted at each time instance from the field test dataset A using the z-dependent ST RMM.

C. DETERMINATION OF THRESHOLD R^{thrd} or R_{xy}^{thrd}

The threshold R^{thrd} (or R_{xy}^{thrd}) has a significant impact on the estimation performance. A smaller threshold leads to shorter travel time intervals and hence better estimation accuracy but worse predictability. A smaller threshold results in higher correlation of turn radii across different travel time intervals, deviating from the independence assumption of turn radii in ST models. In this section, we introduce a systematic approach to select the best threshold R^{thrd} (or R_{xy}^{thrd}) that balances between the *estimation accuracy* and *model predictability*. Here we first introduce two metrics to measure the estimation performance. The threshold selection algorithm then follows.

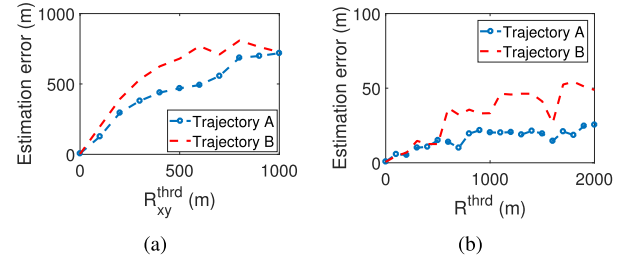


FIGURE 9. Evaluation of the estimation accuracy for the a) z-independent ST RMM with different R_{xy}^{thrd} , and b) z-dependent ST RMM with different R^{thrd} . Both figures are generated using dataset A.

1) EVALUATION OF ESTIMATION ACCURACY

Different metrics can be used to evaluate the estimation accuracy, such as Root Mean Squared Error (RMSE) [40], [41], R -square [42], Sum of Squares due to Error (SSE) [43]. Here, we adopted a modified RMSE metric described by the following equation to penalize large errors at small portions of the trajectories:

$$\text{Error} = \sqrt[4]{\frac{1}{N} \sum_{k=1}^N \|\mathbf{p}[k] - \hat{\mathbf{p}}[k]\|_4^4}$$

where $\|\mathbf{x}\|_4$ represents the l_4 -norm of vector \mathbf{x} and N is the total number of samples in a trajectory. Figure 9 shows the estimation accuracy of the two trajectories with different R^{thrd} (or R_{xy}^{thrd}) using the two 3-D ST RMMs. As expected, small thresholds lead to shorter travel time intervals, and thus small estimation errors and good estimation accuracy. The relationship between the travel time interval and the estimation accuracy is shown in Figure 10(a) generated using example dataset A, where $\bar{\tau} = \frac{\sum_{i=1}^M \hat{\tau}[T_i]}{M}$, and M is the total number of travel time intervals.

As the turn radius $\hat{R}_{xy}[T_i]$ estimated by the z-independent ST RMM is smaller than $\hat{R}[T_i]$ obtained by the z-dependent model (because of the 3-D to 2-D projection), to achieve the same performance, the threshold R_{xy}^{thrd} required by the z-independent ST RMM is also smaller than R^{thrd} required by the z-dependent model. This is further illustrated in Figure 10. As an example, to achieve an estimation accuracy of 20m, $R_{xy}^{thrd} = 34m$ and $R^{thrd} = 800m$ are selected, which lead to mean estimated travel time intervals of 0.54s and 0.31s respectively.

2) EVALUATION OF MODEL PREDICTABILITY

We use the Pearson's correlation coefficient [44] to measure the correlation, ρ , of turn radii in adjacent travel time intervals, as a metric for model predictability.

$$\rho = \frac{\sum_{i=1}^{M-1} (\hat{R}[\hat{T}_i] - \bar{R}_1)(\hat{R}[\hat{T}_{i+1}] - \bar{R}_2)}{\sqrt{\sum_{i=1}^{M-1} (\hat{R}[\hat{T}_i] - \bar{R}_1)^2} \sqrt{\sum_{i=1}^{M-1} (\hat{R}[\hat{T}_{i+1}] - \bar{R}_2)^2}}$$

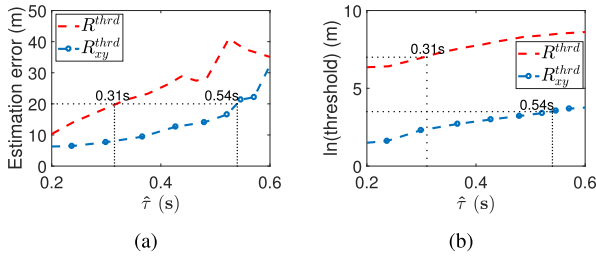


FIGURE 10. Relationship a) between the estimation accuracy and the mean estimated travel time interval $\hat{\tau}$ for the two 3-D ST RMMs, and b) between the threshold R^{thrd} (or R_{xy}^{thrd}) and the mean estimated travel time interval $\hat{\tau}$. Both figures are generated using dataset A.

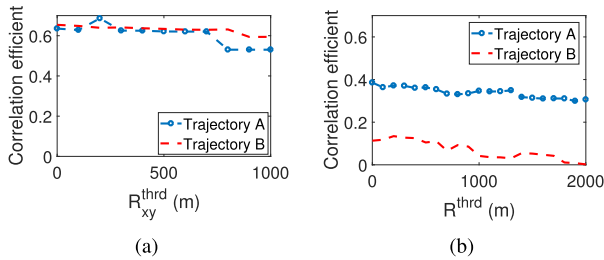


FIGURE 11. Comparison of the correlation coefficient with a) different R^{thrd} in the z-independent ST RMM and b) different R_{xy}^{thrd} z-dependent ST RMM.

where $\bar{R}_1 = \frac{1}{M-1} \sum_{i=1}^{M-1} \hat{R}[\hat{T}_i]$, $\bar{R}_2 = \frac{1}{M-1} \sum_{i=1}^{M-1} \hat{R}[\hat{T}_{i+1}]$. Figure 11 shows the correlation coefficients computed at different values of the thresholds. As expected, ρ decreases with the increase of R^{thrd} (or R_{xy}^{thrd}), indicating an enlarged travel time interval and improved model predictability. In addition, the sustained low correlations observed in the z-dependent ST RMM even at small values of R^{thrd} indicate its good model predictability compared with the z-independent ST RMM.

3) ALGORITHM TO SELECT THRESHOLD R^{thrd} OR R_{xy}^{thrd}

The threshold R^{thrd} (or R_{xy}^{thrd}) is selected using the following two steps to balance the estimation accuracy and model predictability.

- **Step 1:** Find thresholds R^{thrd} (or R_{xy}^{thrd}) with errors less than a constant chosen by users. In this study, we set this value as 20m.
- **Step 2:** Among all thresholds selected in the first step, find the one with the minimum $|\rho|$.

The thresholds selected using the above algorithm for the two trajectories are summarized in Table 2.

D. ESTIMATION AND CONFIGURATION OF RANDOM VARIABLES

We estimate random variables in the RMMs, and in particular their probability density functions (PDFs). The estimated 3-D ST RMMs can be used to generate rich trajectory ensembles. Note that all flight field test data are used to derive the PDFs.

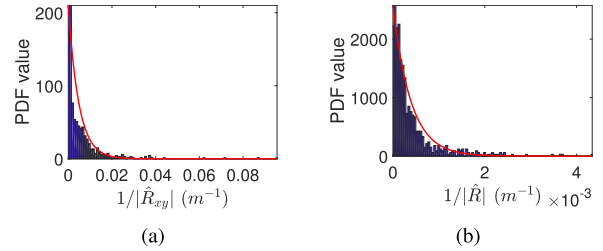


FIGURE 12. PDF of the inverse of turn radius for the a) z-independent and b) z-dependent ST RMMs.

1) TURN RADIUS RANDOM VARIABLE

Turn radius is one of the most important random variables in the RMMs. Appropriate turn radii guarantee safe aerial maneuvers.

By analyzing all $\hat{R}[\hat{T}_i]$ (or $\hat{R}_{xy}[\hat{T}_i]$ for the z-independent ST RMM) data extracted from the two datasets in Section V-B.2, we find that the PDF of $\frac{1}{|\hat{R}|}$ approximately matches with the exponential distribution (see Figure 12). The bias may be caused by the lack of data and effect of smoothing. Due to the structural constraints of aircraft, safe ranges of turn radii need to be imposed. Suppose the safe range of the turn radius $|\hat{R}|$ is $[R_s, \infty)$ (turn radius of ∞ leads to straight trajectories), the PDF of $\frac{1}{|\hat{R}|}$ can be expressed as a truncated exponential distribution:

$$f\left(\frac{1}{|\hat{R}|}\right) = \frac{\lambda_r e^{-\frac{\lambda_r}{|\hat{R}|}}}{1 - e^{-\frac{\lambda_r}{R_s}}}, \quad |\hat{R}| \geq R_s$$

where $\frac{1}{\lambda_r} = E\left(\frac{1}{|\hat{R}|}\right) = \frac{1}{M_1+M_2} \sum_{j=1}^2 \sum_{i=1}^{M_j} \frac{1}{|\hat{R}[\hat{T}_i]|}$. M_j is the total number of travel time intervals in trajectory j , where $j = \{A, B\}$. A larger λ_r indicates a higher possibility to choose a large turn radius, and therefore a straighter trajectory.

The minimum (safe) turn radius, R_s , is dependent on the mechanical structure of an aircraft. In particular, the turn radius is proportional to $\frac{V^2}{n}$, where $n = \frac{L}{g}$ is the load factor measuring an aircraft's structural limits. Therefore, R_s is achieved at the lowest speed for the highest allowable n , which is the corner speed [45]. The maximum load factor varies for different types of aircraft. For instance, for normal and commuter category airplanes, n cannot exceed 3.8 [45], [46].

2) TRAVEL TIME INTERVAL RANDOM VARIABLE

The PDF of the travel time interval $\hat{\tau}$ also approximately matches the exponential distribution with mean $1/\lambda_\tau$ as shown in Figure 13. Similarly, the bias may be caused by the lack of data and effect of smoothing. A constraint can be enforced to avoid frequent changes of turn centers, through a truncated distribution if necessary. We here do not place any constraint on the travel time interval.

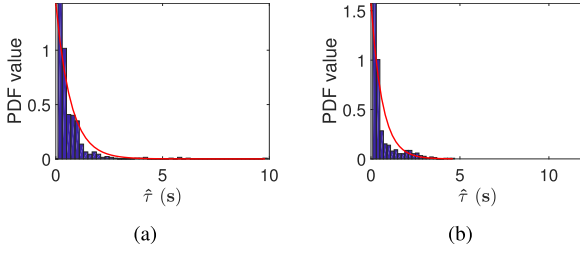


FIGURE 13. PDFs of the travel time interval random variable in the a) z -independent and b) z -dependent ST RMMs.

3) SPEED RANDOM VARIABLE

A similar approach can be used to find the PDFs for the speed \hat{V}_{xy} in the z -independent ST RMM and \hat{V} in the z -dependent ST RMM. Here, we model the correlation of speed over time using a Gauss-Markov model. In particular, we model the speed \hat{V} (or \hat{V}_{xy}) at the i -th travel time interval using the following equation [9], [47], [48]:

$$\hat{V}[\hat{T}_i] = \hat{\gamma} \hat{V}[\hat{T}_{i-1}] + (1 - \hat{\gamma}) \hat{\mu} + \sqrt{(1 - \hat{\gamma}^2)} \hat{D}[\hat{T}_{i-1}] \quad (6)$$

where $0 < \hat{\gamma} < 1$ is a correlation factor, $\hat{\mu}$ is the mean speed as $k \rightarrow \infty$, $\hat{D}[\hat{T}_{i-1}]$ is a random variable following a normal distribution with zero mean and variance $\hat{\sigma}^2$. These parameters are computed for each trajectory using the following equations [40], [47], [48]:

$$\begin{aligned} \hat{\mu} &= \frac{1}{M} \sum_{i=1}^M \hat{V}[\hat{T}_i] \\ \hat{\sigma}^2 &= \frac{1}{M-1} \sum_{i=1}^M (\hat{V}[\hat{T}_i] - \hat{\mu})^2 \\ \hat{\gamma} &= \begin{cases} 1, & \text{if } \hat{\sigma} \approx 0 \\ \max(0, \frac{\hat{\sigma}^2}{\hat{\sigma}^2}), & \text{else} \end{cases} \end{aligned}$$

where $\hat{\sigma}^2 = \frac{1}{M-1} \sum_{i=1}^{M-1} (\hat{V}[\hat{T}_i] - \hat{\mu})(\hat{V}[\hat{T}_{i+1}] - \hat{\mu})$. After we obtain the values of $\hat{\mu}$, $\hat{\sigma}$ and $\hat{\gamma}$ for each dataset, we calculate their averages, denoted as $\bar{\mu}$, $\bar{\sigma}$ and $\bar{\gamma}$, which are used to generate trajectory ensembles. See Table 3 for the values of $\bar{\mu}$, $\bar{\sigma}$ and $\bar{\gamma}$ estimated from the flight field test data.

Due to mechanical constraints, the aircraft's speed should not exceed a certain range. Typically, the speed is minimized at the stall speed [49] and maximized at the Velocity to Never Exceed (VNE) [50]. This speed range constraint can be enforced by modeling $\hat{D}[\hat{T}_{i-1}]$ in Equation (6) as a truncated normal distribution [51], with its range calculated according to the range of the speed and $\hat{V}[\hat{T}_{i-1}]$ at the end of each travel time interval.

4) ALTITUDE RANDOM VARIABLE

In the z -dependent ST RMM, the altitude of the turn center, c_z , is a random variable to be configured. As shown in Equation (5), the range of $c_z[\hat{T}_i]$ depends on the aircraft's altitude $p_z[\hat{T}_i]$, velocity $v[\hat{T}_i]$ and turn radius $R[\hat{T}_i]$. For simplicity, we here model c_z as a uniform random variable,

TABLE 3. Random variables (RV) to be configured.

Model	RV	Parameters	Value
z -independent	R_{xy}	λ_r	210 (m)
	V_{xy}	$\bar{\mu}$	15.34 (m/s)
		$\bar{\sigma}$	2.35
		$\bar{\gamma}$	0.9413
	τ	λ_τ	0.6987 (s)
z -dependent	a_z	λ_a	169.4915 (s^2/m)
	R	λ_r	2577 (m)
		$\bar{\mu}$	15.06 (m/s)
		$\bar{\sigma}$	3.04
		$\bar{\gamma}$	0.98
	τ	λ_τ	0.6349 (s)
	c_z	Uniformly distributed with changing range	

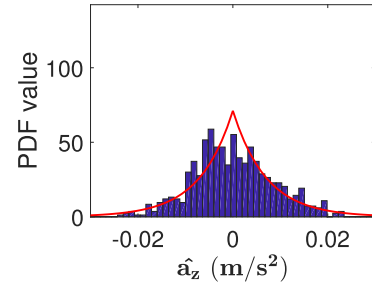


FIGURE 14. PDF of the acceleration along the z direction for the z -independent ST RMM.

the range of which is updated at the end of each travel time interval using Equation (5).

Federal Aviation Administration (FAA) places the altitude constraints for various aircraft, e.g., small UAVs should fly below 400 feet [52]–[55]. We can enforce such altitude constraints through configuring the sizes of the simulation area and the boundary model described in Section IV.

5) ACCELERATION RANDOM VARIABLE

The vertical acceleration a_z needs to be configured in the z -independent ST RMM. Using all acceleration data extracted from the two datasets, we plot the PDF of \hat{a}_z in Figure 14, which approximately matches with a double exponential distribution. The bias may be caused by the lack of data. As \hat{a}_z impacts the vertical speed and altitude of the aircraft, a range constraint should be enforced to ensure that the vertical speed and altitude do not exceed their bounds. Suppose \hat{a}_z should remain in the range of $[a_{zmin}, a_{zmax}]$, its PDF can be described by a truncated double exponential distribution

$$f(\hat{a}_z) = \begin{cases} \frac{\lambda_a e^{-\lambda_a \hat{a}_z}}{2(1 - e^{\lambda_a a_{zmax}})}, & \text{if } 0 \leq \hat{a}_z \leq a_{zmax} \\ \frac{\lambda_a e^{\lambda_a \hat{a}_z}}{2(1 - e^{-\lambda_a a_{zmin}})}, & \text{if } a_{zmin} \leq \hat{a}_z < 0 \end{cases}$$

where $\frac{1}{\lambda_a} = \frac{1}{M_1 + M_2} \sum_{j=1}^2 \sum_{i=1}^{M_j} \hat{a}_z[\hat{T}_i]$.

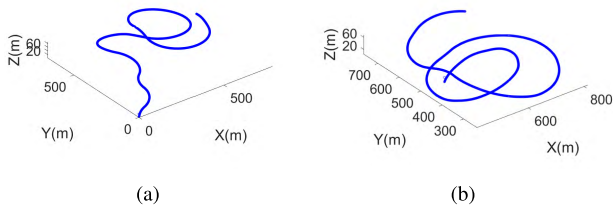


FIGURE 15. Example random trajectories generated by the a) z -independent and b) z -dependent ST RMM.

Now let's determine the range $[a_{zmin}, a_{zmax}]$. Note that although the altitude is impacted by \hat{a}_z , its range constraint can be satisfied through restricting the simulation area. Therefore, we only need to consider the impact of \hat{a}_z on the vertical speed \hat{v}_z . Suppose the vertical speed of the aircraft cannot exceed the range $[v_{zmin}, v_{zmax}]$, then the bounds of $\hat{a}_z[\hat{T}_i]$ satisfy the following equations

$$a_{zmax} = \frac{v_{zmax} - \hat{v}_z[\hat{T}_i]}{\hat{t}_{i-1}} \geq 0$$

$$a_{zmin} = \frac{v_{zmin} - \hat{v}_z[\hat{T}_i]}{\hat{t}_{i-1}} \leq 0$$

which are updated at the end of each travel time interval.

E. RANDOM TRAJECTORY GENERATION

Table 3 lists the estimated values of the parameters for the random variables in the RMMs. The ranges of turn radius and speed for the z -independent ST RMM are set to $|R_{xy}| \in (10.4637m, \infty)$, $V_{xy} \in [3.98m/s, 23.01m/s]$ and $v_z \in [0.00027m/s, 0.1580m/s]$ respectively. For the z -dependent ST RMM, we set $|R| \in (210.1077m, \infty)$ and $V \in [3.74m/s, 23.04m/s]$. The size of the simulation area is set to $1000m \times 1000m \times 100m$. With the estimated parameters, we can generate rich trajectory ensembles with the same statistics as the original flight test data. Figure 15 shows the example trajectories generated from the configured 3-D ST RMMs.

F. DISCUSSIONS

Various other distribution models can be used to model the aforementioned random variables to meet different application requirements. For example, in the SRCM model [15], the turn radius is randomly chosen from a set of uniformly-spaced constants for search and rescue purposes. The selection of turn radius, travel time interval, or acceleration can also be modeled as correlated across time, using a similar approach as described in Equation (6).

VI. CONCLUSION

In this paper, we introduced two 3-D Smooth-Turn (ST) random mobility models (RMMs) to facilitate the design and evaluation of airborne networks (ANs). Both models are extended from the basic 2-D ST RMM, but differ in motion

patterns along the z direction. In particular, the aerial mobility along the z direction is assumed to be independent from the other two dimensions in the z -independent ST RMM, while dependent in the z -dependent ST RMM. The z -independent ST RMM is more suitable for applications with less variation in aerial mobility along the z direction, such as civilian and commercial applications; while the z -dependent ST RMM is suitable for applications involving climbing or descending turns, such as military applications and air shows. Realistic boundary models have also been developed to model the aerial mobility near the boundary of the simulation area. We developed a systematic procedure to estimate and configure parameters of the random variables in the proposed models, and illustrated the procedure step-by-step using real flight field test data. The good match between the estimated and real trajectories suggests the promising performance of proposed models and estimation methods in capturing smooth aerial turns. In the future, we will conduct networking performance analysis on the RMM-based UAV swarms that are subject to collision avoidance protocols.

ACKNOWLEDGMENT

We sincerely acknowledge Michael W. Menard, Maurice Griffin, Thomas Frierson, Tye Payne, and Mike Menard from the Lone Star UAS Center of Excellence (LSUASC) for providing the flight field test data used in this paper. Some prior works developed for this paper are documented in [56] and [57]. We would also like to thank Gilbert L. Peterson and John F. Raquet and Kamesh Namuduri for the flight field test data set used in [56].

REFERENCES

- [1] J. Ahrenholz, "Comparison of core network emulation platforms," in *Proc. IEEE Military Commun. Conf.*, San Jose, CA, USA, Oct./Nov. 2010, pp. 166–171.
- [2] J. Ahrenholz, C. Danilov, T. R. Henderson, and J. H. Kim, "CORE: A real-time network emulator," in *Proc. Military Commun. Conf.*, San Diego, CA, USA, Nov. 2010, pp. 1–7.
- [3] G. F. Riley and T. R. Henderson, "The ns-3 network simulator," in *Modeling and Tools for Network Simulation*. Heidelberg, Germany: Springer, 2010, pp. 15–34.
- [4] *Opnet*. Accessed: Apr. 24, 2018. [Online]. Available: <http://www.opnet.com/>
- [5] B. N. Cheng and S. Moore, "A comparison of MANET routing protocols on airborne tactical networks," in *Proc. Military Commun. Conf. (MILCOM)*, Oct. 2012, pp. 1–6.
- [6] Y. Cheng, E. K. Çetinkaya, and J. P. G. Sterbenz, "Performance comparison of routing protocols for transactional traffic over aeronautical networks," in *Proc. Int. Telemetering Conf.*, Bally's Las Vegas NV, USA, Oct. 2011, pp. 1–10.
- [7] L. Lin, Q. Sun, J. Li, and F. Yang, "Novel geographic position mobility oriented routing strategy for UAVs," *J. Comput. Inf. Syst.*, vol. 8, no. 2, pp. 709–716, 2012.
- [8] K. Peters, E. K. Çetinkaya, A. Jabbar, and J. P. G. Sterbenz, "Analysis of a geolocation-assisted routing protocol for airborne telemetry networks," in *Proc. Int. Telemetering Conf.*, San Diego, CA, USA, Oct. 2010, pp. 1–10.
- [9] J. P. Rohrer, E. K. Çetinkaya, H. Narra, D. Broyles, K. Peters, and J. P. G. Sterbenz, "AeroRP performance in highly-dynamic airborne networks using 3D Gauss–Markov mobility model," in *Proc. Military Commun. Conf.*, Baltimore, MD, USA, Nov. 2011, pp. 834–841.
- [10] T. Camp, J. Boleng, and V. Davies, "A survey of mobility models for ad hoc network research," *Wireless Commun. Mobile Comput.*, vol. 2, no. 5, pp. 483–502, Sep. 2002.

- [11] K. Pearson, "The problem of the random walk," *Nature*, vol. 72, p. 294, Jul. 1905.
- [12] C. Bettstetter, H. Hartenstein, and X. Pérez-Costa, "Stochastic properties of the random waypoint mobility model," *Wireless Netw.*, vol. 10, no. 5, pp. 555–567, 2004.
- [13] B. Gloss, M. Scharf, and D. Neubauer, "A more realistic random direction mobility model," in *Proc. TD*, 2005, pp. 1–12.
- [14] P. Nain, D. Towsley, B. Liu, and Z. Liu, "Properties of random direction models," in *Proc. IEEE 24th Annu. Joint Conf. IEEE Comput. Commun. Soc. (INFOCOM)*, vol. 3. Miami, FL, USA, Mar. 2005, pp. 1897–1907.
- [15] W. Wang, X. Guan, B. Wang, and Y. Wang, "A novel mobility model based on semi-random circular movement in mobile ad hoc networks," *Inf. Sci.*, vol. 180, no. 3, pp. 399–413, 2010.
- [16] E. Kuiper and S. Nadjm-Tehrani, "Geographical routing with location service in intermittently connected MANETs," *IEEE Trans. Veh. Technol.*, vol. 60, no. 2, pp. 592–604, Feb. 2011.
- [17] E. Kuiper and S. Nadjm-Tehrani, "Mobility models for UAV group reconnaissance applications," in *Proc. IEEE Int. Conf. Wireless Mobile Commun.*, Bucharest, Romania, Jul. 2006, p. 33.
- [18] E. Kuiper, "Mobility and routing in a delay-tolerant network of unmanned aerial vehicles," M.S. thesis, Dept. Comput. Inf. Sci., Linköping Univ., Linköping, Sweden, 2008.
- [19] Y. Wan, K. Namuduri, Y. Zhou, D. He, and S. Fu, "A smooth-turn mobility model for airborne networks," in *Proc. 1st ACM MobiHoc Workshop Airborne Netw. Commun.*, Hilton Head, SC, USA, Jun. 2012, pp. 25–30.
- [20] Y. Wan, K. Namuduri, Y. Zhou, and S. Fu, "A smooth-turn mobility model for airborne networks," *IEEE Trans. Veh. Technol.*, vol. 62, no. 7, pp. 3359–3370, Sep. 2013.
- [21] Y. Zhu, Q. Huang, J. Li, and D. Wu, "Design and evaluation of airborne communication networks," in *Proc. 7th Int. Conf. Ubiquitous Future Netw. (ICUFN)*, Sapporo, Japan, Jul. 2015, pp. 277–282.
- [22] A. Bujari, C. T. Calafate, J.-C. Cano, P. Manzoni, C. E. Palazzi, and D. Ronzani, "Flying ad-hoc network application scenarios and mobility models," *Int. J. Distrib. Sensor Netw.*, vol. 13, no. 10, pp. 1–17, 2017.
- [23] J.-D. M. Biomo, "Unmanned aeronautical ad-hoc networks: Enhancing the reactive-greedy-reactive protocol and introducing a new mobility model," Ph.D. dissertation, Carleton Univ. Ottawa, Ottawa, ON, Canada, 2014.
- [24] A. Tiwari et al., "Mobility aware routing for the airborne network backbone," in *Proc. Military Commun. Conf.*, San Diego, CA, USA, Nov. 2008, pp. 1–7.
- [25] K. Sampigethaya, R. Poovendran, S. Shetty, T. Davis, and C. Royalty, "Future E-enabled aircraft communications and security: The next 20 years and beyond," *Proc. IEEE*, vol. 99, no. 11, pp. 2040–2055, Nov. 2011.
- [26] J. Xie, Y. Wan, J. H. Kim, S. Fu, and K. Namuduri, "A survey and analysis of mobility models for airborne networks," *IEEE Commun. Surveys Tuts.*, vol. 16, no. 3, pp. 1221–1238, 3rd Quart., 2014.
- [27] *Cruise Performance Theory*. Accessed: Apr. 24, 2018. [Online]. Available: <http://www.dtic.mil/get-tr-doc/pdf?AD=ADA320213>
- [28] *Bank Angle and the Physics of Standard Rate Turns*. [Online]. Available: http://www.luizmonteiro.com/Article_Bank_Angle_for_Std_Rate_01.aspx
- [29] H. W. Glauert, *The Elements of Aerofoil and Airscrew Theory*. Cambridge, U.K.: Cambridge Univ. Press, 1947.
- [30] *Forces in a Climb*. Accessed: Apr. 24, 2018. [Online]. Available: <http://www.grc.nasa.gov/WWW/k-12/airplane/climb.html>
- [31] *All Types of Turns*. Accessed: Apr. 24, 2018. [Online]. Available: <https://www.aopa.org/training-and-safety/students/presolo/skills/all-types-of-turns>
- [32] X. R. Li and V. P. Jilkov, "Survey of maneuvering target tracking: Dynamic models," *Proc. SPIE*, vol. 4048, pp. 212–236, Apr. 2000.
- [33] L. A. Weitz, "Derivation of a point-mass aircraft model used for fast-time simulation," MITRE, McLean, Va, USA, Tech. Rep. MTR150184, 2015.
- [34] R. F. Berg, "Estimation and prediction for maneuvering target trajectories," *IEEE Trans. Autom. Control*, vol. AC-28, no. 3, pp. 294–304, Mar. 1983.
- [35] D. Broyles, A. Jabbar, and J. P. G. Sterbenz, "Design and analysis of a 3D Gauss–Markov mobility model for highly dynamic airborne networks," in *Proc. Int. Telemetering Conf.*, San Diego, CA, USA, Oct. 2010, pp. 1–10.
- [36] S. Drake, "Converting GPS coordinates [ϕ λ h] to navigation coordinates (ENU)," DSTO Electron. Surveill. Res. Lab., Tech. Rep., 2002.
- [37] C.-Y. King, "Virtual instrumentation-based system in a real-time applications of GPS/GIS," in *Proc. IEEE Int. Conf. Recent Adv. Space Technol.*, Istanbul, Turkey, Nov. 2003, pp. 403–408.
- [38] *Geodetic Datum*. Accessed: Apr. 24, 2018. [Online]. Available: http://en.wikipedia.org/wiki/Geodetic_datum
- [39] T. O'Haver. (Jan. 2001). *Smoothing*. [Online]. Available: http://en.wikipedia.org/wiki/Geodetic_datum
- [40] B.-H. Liu, M.-L. Chen, and M.-J. Tsai, "Message-efficient location prediction for mobile objects in wireless sensor networks using a maximum likelihood technique," *IEEE Trans. Comput.*, vol. 60, no. 6, pp. 865–878, Jun. 2011.
- [41] N. Nabaa and R. H. Bishop, "Validation and comparison of coordinated turn aircraft maneuver models," *IEEE Trans. Aerosp. Electron. Syst.*, vol. 36, no. 1, pp. 250–259, Jan. 2000.
- [42] A. C. Cameron and F. A. Windmeijer, "An R-squared measure of goodness of fit for some common nonlinear regression models," *J. Econ.*, vol. 77, no. 2, pp. 329–342, 1997.
- [43] D. Kleinbaum, L. Kupper, A. Nizam, and E. Rosenberg, *Applied Regression Analysis and Other Multivariable Methods*. Toronto, ON, Canada: Nelson Education, 2013.
- [44] J. L. Rodgers and W. A. Nicewander, "Thirteen ways to look at the correlation coefficient," *Amer. Statist.*, vol. 42, no. 1, pp. 59–66, 1988.
- [45] *Maneuvering Loads, High-G Maneuvers*. Accessed: Apr. 24, 2018. [Online]. Available: http://www.flightlab.net/Flightlab.net/Download_Course_Notes_files/8_Maneuvering.pdf
- [46] *FAA Federal Aviation Regulations (FARS, 14CFR)*. Accessed: Apr. 24, 2018. [Online]. Available: http://www.flightsimulation.com/data/FARS/part_23-337.html
- [47] B. Liang and Z. Haas, "Predictive distance-based mobility management for PCS networks," in *Proc. Proc. 18th Annu. Joint Conf. IEEE Comput. Commun. Soc. (INFOCOM)*, vol. 3. New York, NY, USA, Mar. 1999, pp. 1377–1384.
- [48] B. Liang and Z. J. Haas, "Predictive distance-based mobility management for multidimensional PCS networks," *IEEE/ACM Trans. Netw.*, vol. 11, no. 5, pp. 718–732, Oct. 2003.
- [49] *Stall (Flight)*. Accessed: Apr. 24, 2018. [Online]. Available: [http://en.wikipedia.org/wiki/Stall_\(flight\)](http://en.wikipedia.org/wiki/Stall_(flight))
- [50] P. E. Illman and G. E. Gailey, *The Pilot's Handbook of Aeronautical Knowledge*. New York, NY, USA: McGraw-Hill, 2000.
- [51] *Truncated Normal Distribution*. Accessed: Apr. 24, 2018. [Online]. Available: https://en.wikipedia.org/wiki/Truncated_normal_distribution
- [52] *Minimum Safe Altitude*. Accessed: Apr. 24, 2018. [Online]. Available: <http://www.risingup.com/fars/info/part91-119-FAR.shtml>
- [53] *Minimum Altitudes for IFR Operations*. Accessed: Apr. 24, 2018. [Online]. Available: <http://www.risingup.com/fars/info/part91-177-FAR.shtml>
- [54] *VFR Cruising Altitude or Flight Level*. Accessed: Apr. 24, 2018. [Online]. Available: <http://www.risingup.com/fars/info/part91-159-FAR.shtml>
- [55] *Summary of Small Unmanned Aircraft Rule (Part 107)*. Accessed: Apr. 24, 2018. [Online]. Available: https://www.faa.gov/uas/media/Part_107_Summary.pdf
- [56] J. Xie, Y. Wan, K. Namuduri, S. Fu, G. L. Peterson, and J. F. Raquet, "Estimation and validation of the 3D smooth-turn mobility model for airborne networks," in *Proc. Military Commun. Conf.*, San Diego, CA, USA, Nov. 2013, pp. 556–561.
- [57] J. Xie, Y. Wan, K. Namuduri, S. Fu, and J. Kim, "A comprehensive modeling framework for airborne mobility," in *Proc. AIAA Infotech Aerosp. Conf.*, Boston, MA, USA, Aug. 2013, pp. 5053–5062.



JUNFEI XIE (S'13–M'16) received the B.S. degree in electrical engineering from the University of Electronic Science and Technology of China, Chengdu, China, in 2012, and the M.S. degree in electrical engineering and the Ph.D. degree in computer science and engineering from the University of North Texas, Denton, TX, USA, in 2013 and 2016, respectively. She is currently an Assistant Professor with the Department of Computing Sciences, Texas A&M University-Corpus Christi. Her current research interests include large-scale dynamic system design and control, managing and mining big spatiotemporal data, airborne networks, complex information system, and air traffic flow management.



YAN WAN (S'08–M'09–SM'17) received the Ph.D. degree in electrical engineering from Washington State University in 2008. She completed the Postdoctoral training from the University of California at Santa Barbara, Santa Barbara. From 2009 to 2016, she was an Assistant Professor and an Associate Professor with the University of North Texas. She is currently an Associate Professor with the Electrical Engineering Department, The University of Texas at Arlington.

Her research interests lie in the modeling, evaluation and control of large-scale dynamical networks, cyber-physical system, stochastic networks, decentralized control, learning control, networking, uncertainty analysis, algebraic graph theory, and their applications to UAV networking, UAV traffic management, epidemic spread, complex information networks, and air traffic management. Her research has led to over 130 publications and successful technology transfer outcomes. She has been recognized by several prestigious awards, including the NSF CAREER Award, RTCA William E. Jackson Award, and the U.S. Ignite and GENI demonstration awards. She is currently the Vice President of the IEEE Comsoc Fort Worth Chapter and Technical Committee Member of AIAA Intelligent Systems Society. She is also the Associate Editor of the *TRANSACTIONS OF THE INSTITUTE OF MEASUREMENT AND CONTROL*.



BAOQIAN WANG received the B.S. degree from Yangtze University, Wuhan, China, in 2017. He is currently pursuing the Ph.D. degree with the Department of Computing Sciences, Texas A&M University-Corpus Christi. His research interests include unmanned aircraft systems, airborne networks, and virtualization techniques.



SHENGLI FU (S'01–M'04–SM'07) received the B.S. and M.S. degrees in telecommunication engineering from the Beijing University of Posts and Telecommunications, Beijing, China, in 1994 and 1997, respectively, the M.S. degree in computer engineering from Wright State University, Dayton, OH, USA, in 2002, and the Ph.D. degree in electrical engineering from the University of Delaware, Newark, DE, USA, in 2005. He is currently a Professor and the Chair of the Department of Electrical Engineering, University of North Texas, Denton, TX, USA. His research interests include coding and information theory, wireless communications and sensor networks, and aerial networks.

His research interests include coding and information theory, wireless communications and sensor networks, and aerial networks.



KEJIE LU (S'01–M'04–SM'07) received the B.Sc. and M.Sc. degrees in telecommunications engineering from the Beijing University of Posts and Telecommunications, Beijing, China, in 1994 and 1997, respectively, and the Ph.D. degree in electrical engineering from The University of Texas at Dallas in 2003. In 2004 and 2005, he was a Post-Doctoral Research Associate with the Department of Electrical and Computer Engineering, University of Florida. In 2005, he joined the University

of Puerto Rico, Mayagüez, where he is currently a Professor. His research interests include architecture and protocols design for computer and communication networks, performance analysis, network security, and wireless communications.



JAE H. KIM has been a Principal Investigator and a Program Manager for a number of U.S. Department of Defense contract programs from DARPA, Army CERDEC, Air Force AFRL, Navy ONR, and NASA. He has been a Senior Research Scientist and a Project Manager with the NASA Jet Propulsion Laboratory, California Institute of Technology, since 1987. He has been serving as an Affiliate Professor and a Graduate Faculty of the Electrical and Computer Engineering Department,

University of Washington, Seattle, WA, USA, since 2000. He has also served as an IEEE Associate Editor for a monthly *Technical Journal of Communications Letters* for a decade since 2001. He is currently an Executive Senior Technical Fellow of the Boeing Research & Technology in the area of communications and network systems.

His research area of interests is wireless communications and mobile networking, with specific interests in adaptive MANET, UAV-based airborne internetworking, resilient NetOps with auto-configuration and distributed information services, and spectrum and jamming-aware MANET under extreme contested environments. He is currently developing Software Defined Network at Tactical Edge and the unified networking framework across heterogeneous networks using contents-aware Universal Messaging System.

He received the B.S. and M.S. degrees from Seoul National University, and the Ph.D. degree from the University of Florida, Gainesville, all in electrical and computer engineering. He has authored or co-authored over 100 publications, eight U.S. Patents (six granted and two pending). He co-edited two books, *Green IT: Technologies and Applications*, (Springer-Verlag, in 2011) and *UAV Networks and Communications*, (Cambridge University Press, in 2017). He was a recipient of 10 NASA Technical Innovation Awards and over 25 Boeing Technology Awards for outstanding technical performance recognition.

...